Science Arts & Métiers (SAM)
is an open access repository that collects the work of Arts et Métiers Institute of Technology researchers and makes it freely available over the web where possible.

This is an author-deposited version published in: https://sam.ensam.eu
Handle ID: .http://hdl.handle.net/10985/22237

To cite this version :

Xiaoyu LIANG, Anis HOR, Camille ROBERT, Mehdi SALEM, Feng LIN, Franck MOREL - High cycle fatigue behavior of 316L steel fabricated by laser powder bed fusion: Effects of surface defect and loading mode - International Journal of Fatigue - Vol. 160, p.106843 - 2022

Any correspondence concerning this service should be sent to the repository Administrator : scienceouverte@ensam.eu

High cycle fatigue behavior of 316L steel fabricated by laser powder bed fusion: Effects of surface defect and loading mode

Xiaoyu Liang [a,b,c,*], Anis Hor [b], Camille Robert [a], Mehdi Salem [b], Feng Lin [c], Franck Morel [a]

[a] Angers Laboratory of Mechanics, Manufacturing Process and innovAtion (LAMPA), Arts et Métiers Campus Angers, 49035 Angers Cedex, France
[b] Institut Clément Ader (ICA), Université de Toulouse, CNRS, ISAE-SUPAERO, UPS, INSA, Mines-Albi, 3 rue Caroline Aigle, 31400 Toulouse, France
[c] Department of Mechanical Engineering, Tsinghua University, 100084 Beijing, China

Keywords:
Laser powder bed fusion
Stainless steel 316L
High cycle fatigue
Surface roughness
Loading mode

A B S T R A C T

The mechanical performances of additive manufactured (AM) material are highly dependent on the fabrication process which inevitably results in surface imperfection as well as porosity. In the present study, the high cycle fatigue (HCF) behavior of an AM stainless steel 316L is experimentally investigated to characterize and evaluate the effect of the inherent surface defects. Profilometry and Computed Tomography are used. A series of fatigue experiments is carried out under different loading modes including tension, bending, and torsion fatigue tests. For each loading condition, different surface preparations are used to investigate the effect of surface state. Fatigue tests reveal that surface treatment can improve fatigue performances, the improvements observed being higher under tension/bending loading than under torsion loading. The fractographic analysis is performed for all the available tested specimens to reveal the mechanism of fatigue crack initiation. Lack-of-fusion (LoF) defects play the predominant role in the fatigue performance of SS 316L fabricated by laser powder bed fusion (LPBF). The presence of multiple LoF defects at the surface or subsurface is detrimental to the endurance under cyclic loading. By using Murakami approach modeling the relationship between fatigue strength and defect size, it is found that the multiple clustering defects act synergistically as one large virtual crack to initiate the fatigue crack.

1. Introduction

Laser powder bed fusion (LPBF), also known as selective laser melting (SLM), has attracted extensive interest because of its high precision of production. LPBF has been successfully applied to many different kinds of metallic materials [1]. Among these materials, stainless steel (SS) 316L is one of the most studied because of its wide applications in the industry due to its good corrosion resistance and superior comprehensive mechanical performances. Characterizing and analyzing LPBF SS 316L has been a hot topic in recent years [2–5]. With regard to the fatigue behavior of LPBF 316L, previous researches have been reported in the literature concerning many aspects: the surface finish [6–11], the heat-treatment [12–15], the building directions [15–17], and certain process parameters [18,19].

Surface finish has been long known to influence the fatigue properties at the first order. The un-melted particles stuck on the surface and unstable melt pool aggravate the surface roughness of LPBF steels [20]. The as-built surface roughness can be optimized but not eliminated via the laser contour parameters [21], the part position, orientation [22], and powder size distribution [23]. The occurrence of porosity or unmelted particles in powder bed fusion parts, especially at or near the surface, has also been shown to be harmful to structural integrity. In addition, post-manufacturing processes, such as machining and polishing, may not always be feasible for AM products, for example in the case of a complex component with inner flow channels. Moreover, surface treatment is time-consuming and increases the global cost of additively manufactured parts. In some medical applications, parts having rougher surfaces are also more prone to assist cohesion between the patient's bone/tissue and AM orthopedic implants than the smooth parts [24,25]. Therefore, it is absolutely necessary to characterize the effect of surface finish on the fatigue performance of AM materials.

An overview of fatigue data from literature with the different surface treatments of LPBF 316L is provided in Fig. 1. As could be expected, mechanical surface treatment improves the fatigue properties of LPBF steels. This improvement is more pronounced in the HCF regime than in the LCF regime. It is consistent with the fact that HCF is more affected by

* Corresponding author at: Department of Mechanical Engineering, Tsinghua University, 100084 Beijing, China
E-mail addresses: liang.xiaoyu@outlook.com, Xiaoyu.LIANG@ensam.eu (X. Liang).

https://doi.org/10.1016/j.ijfatigue.2022.106843

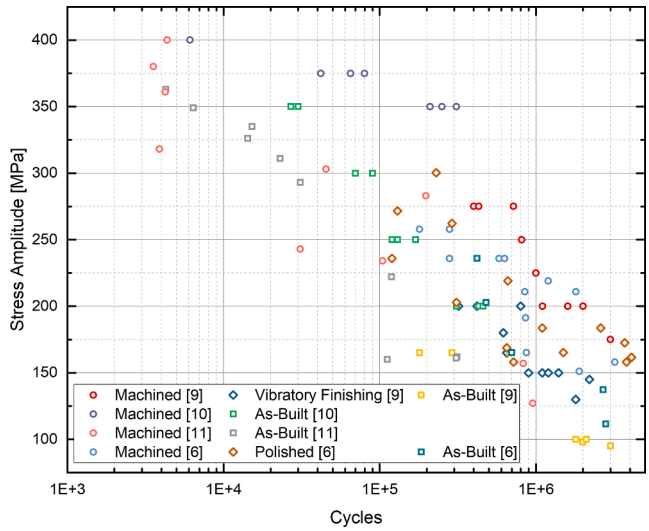

Fig. 1. S-N plots for vertically built LPBF 316L with different surface treatments (data from [6,9–11]; data in [6] are normalized to R = −1 using the Goodman Equation).

the surface quality than LCF [20]. Machining is often adopted as the treatment to eliminate surface roughness whilst it seems to be contradictory to the idea of the net-shape process of AM. As a ductile material, 316L is easily plastically deformed by surface machining and strong residual stress can be introduced. It is hence difficult to decouple the effects of the introduced residual stress and the removed surface imperfections. It should be pointed out that experimental results from AM materials should be compared with cautions as the fabrication and post-treatment procedures may vary. For wrought 316L, it is not surprising that the fatigue strength under bending or tension loading can reach more than 200 MPa [26–28]. The general unsatisfying fatigue performances, even if they are scattered, of the LPBF 316L are worth noting. The enumerated data shown in Fig. 1 provided various fatigue strengths at the 2 millionth cycle and they were inferior to the references of wrought 316L in general. Inherent defects such as lack-of-fusion (LoF) have been mentioned frequently as the trigger of crack initiation, especially in the vertically built samples [11]. Generally, in regard to the whole fabricated sample, insufficient energy input during the PBF process may lead to LoF defects whilst excessive energy input may reduce the presence of LoF defect but bring more gas pores [29]. Nevertheless, the fusion-solidification in the melt pool is a local and transient process that is strongly dependent on the scanning pattern and the part's geometry. There will be hardly a set of processing parameters to ensure suitable energy inputs at each place all over the part. LoF defects are thus currently intrinsic for PBF materials. Knowing that the as-built LPBF materials are often defect-containing, the role of the defect in HCF in different situations should be fully explored.

Previous investigations concerning the fatigue behavior of LPBF 316L are mostly performed under uniaxial tension loading with some under bending loading while torsional fatigue behavior has been less investigated. To date, torsional fatigue tests for LPBF 316L have been seldomly mentioned in the existing literature [30,31]. In empirical knowledge, for the wrought ductile metallic materials, the uniaxial fatigue strength is higher than the torsional fatigue strength and the ratio between uniaxial fatigue strength and torsional fatigue strength for steels is about 1.67 which is close to the ratio $\sqrt{3}$ predicted by the Von Mises criterion [32]. The presence of large defects may lead to the decrease of that ratio, i.e., the uniaxial fatigue strength will be close to the torsional fatigue strength. This may be the case with LPBF metallic materials. Zhang and Fatemi [33] have conducted uniaxial tension and uniaxial torsion fatigue tests for AM Ti-6Al-4V in as-built and surface-treated states. It is reported that the AM samples perform better under torsion loading than under tension loading at the same stress amplitude. This phenomenon was attributed to the inherent defects from the AM process. Besides, for Ti-6Al-4V, it is found that brittle fracture of AM specimens was observed with cracking on the maximum tensile plane, and ductile fracture of wrought specimens with shear cracking [34]. The investigation reported by Wang et al. mentioned that for machined LPBF 316L, the crack initiation phase in the tested AM stainless steel was seen to be Mode II dominated from surface/subsurface defects, and conventional Stage I initiation mechanism was followed by a Mode I governed Stage II process under both tension and torsion loadings [31]. But detailed explanations about crack-initiating defects were not provided. Further study about the relationship between inherent defects and fatigue performances under different loading modes will be essential to promote the industrial application of LPBF 316L.

To offer more insight into the industrial application of this material, the current study aims to investigate the properties of LPBF 316L with a focus on fatigue behavior. We study the material in the as-built state and use only hand-polishing procedures for comparison purposes. The specimens have been thoroughly characterized in terms of residual stress, surface roughness, and porosity. Besides the frequently adopted bending and tension tests, torsion fatigue tests that have seldomly been reported in the literature are also performed. Fractography observations are conducted to better reveal the mechanism of fatigue behavior. The experimental efforts made concerning material preparation, fabrication, and characterization as well as the fatigue-related investigations are detailed. The relationship between fatigue strengths and observed defects at the crack initiation sites is discussed.

2. Material preparation and characterization

2.1. Specimen elaboration

The material studied is the 316L stainless steel (SS). The specimens used in this study were produced by the company PRISMADD (currently Weare Group) using an industrial manufacturing and post-treatment protocol. It should be noted that this protocol consists in using recycled powder of which the oxygen rate is no greater than 1000 ppm. The machine ProX DMP 320 was used with optimized process parameters for 316L SS (listed in Table 1). Generally, the specimens used in the literature often experience contouring since it is a default configuration for most of the LPBF machines. This process step can improve the surface state. In our study, as we try to focus on the surface state effect, a choice is made to skip the contouring step and hence to work with high roughness for the as-built configuration. In this way, surface effect can be emphasized so as to imitate the most unfavorable case of defect presence. Two trays of around 80 specimens consisting of bending, tension, and torsional fatigue samples, as well as some small cylindrical bars for characterization tests, were manufactured with the same process parameters shown in Fig. 2. The above-mentioned specimens were all vertically built, i.e., the axis oriented along the vertical direction. Despite that the gauge zones of the three different types of fatigue specimens are not equivalent in volume, the size effect is expected to be negligible which can be further attested by the obtained SN curves with low dispersion.

A stress-relieving (SR) treatment was carried out aiming to reduce or remove the residual stresses without modifying the microstructures or mechanical properties. It consisted of a temperature holding of 620 °C for 90 min followed by a natural cooling for 800 min until the temperature drops to 180 °C in the air atmosphere without environment control. This SR treatment is similar to those in several previous investigations in the literature [13,17].

Table 1
LPBF process parameters used for specimen's fabrication.

Machine ProX DMP 320	Energetic parameters Laser spot diameter	Scanning speed	Laser Power	Hatch spacing	Layer thickness	Scanning strategy Laser trajectory	Contouring	Angle between successive layers
	0.07 mm	700 mm/s	275 W	0.1 mm	0.05 mm	Random island	No	66°

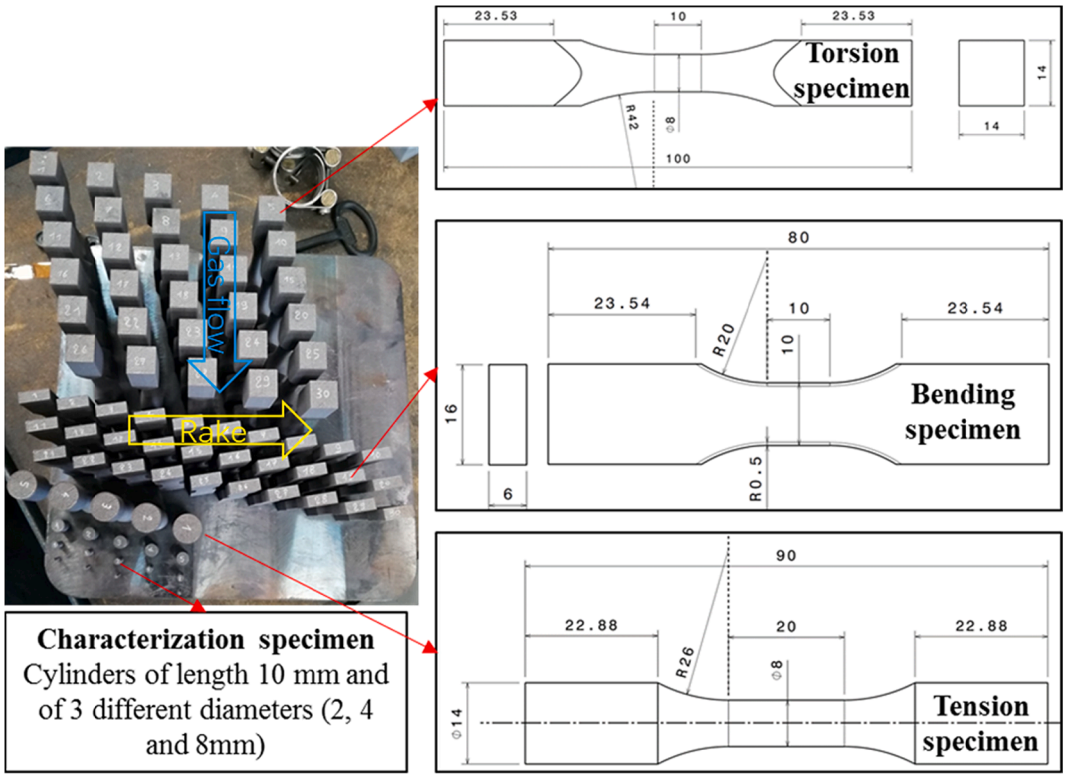

Fig. 2. One fabricated tray with the geometries of specimens (dimensions in mm): Characterization specimens (microstructure); Tension specimens (cyclic behavior and fatigue); Bending specimens (fatigue); Torsion specimens (fatigue).

Table 2
Surface residual stress values after stress releasing heat treatment for the studied specimens and corresponding XRD analysis parameters.

		σ_{11} [MPa]	σ_{22} [MPa]	τ_{12} [Mpa]
Bending Sample 2	4 points averaged for each sample	138	77	2
Bending Sample 16		166	67	−1
Bending Sample 27		105	59	6
Torsional Sample 6	8 points averaged for each sample	120	–	3
Torsional Sample 13		134	–	1
Torsional Sample 18		145	68	3
Anode:		Mn Kalpha	Filter:	Chromium
Anisotropy coefficient (ARX):		1.79	Number of directions:	19
Counting time:		60 s	U	20 kV
Diffraction angle (2θ):		152°	I	1 mA
{h k l} plane:		{3 1 1} (Fe(γ))		

2.2. Specimen characterizations

2.2.1. Residual stress

Compressive surface residual stress is beneficial to the fatigue crack initiation resistance while tensile residual stress reduces the fatigue strength. The surface residual stresses resulting from the LPBF process were analyzed after the stress releasing heat treatment by the X-ray diffraction method. A collimator is used to obtain a beam diameter of 2 mm. Diffraction peaks obtained were then analyzed after a fitting procedure using a Lorentzian function. The conventional $\sin^2(\psi)$ method was applied to obtain the value of the normal and the shear stresses according to the studied direction and plane. The configuration parameters and obtained results are summarized in Table 2. It is found that the heat treatment did not relieve completely surface residual stresses: the σ_{11} component (along building direction) is in a range of 100–200 MPa while the σ_{22} component (perpendicular to building direction) varies from 50 to 100 MPa and the shear stress is zero everywhere. Even though the residual stress is not eliminated by the mentioned stress-relieving heat treatment, the stress level is of low magnitude.

2.2.2. Surface roughness

Since defects are inevitable in the AM process, it is of interest to characterize and quantify the inherent surface and volume defects generated by LPBF. Surface roughness in LPBF parts is mainly attributed to the stair-stepping effect of layer by layer process, partially melted particles attached to the surface, and instability of the melt pool [35,36]. Independently from the alloy, surface roughness can be reduced by increasing the heat input. Yet, extremely high heat input can lead to defect appearance because of high thermal stresses. Adding to that, the powder grades influence the surface roughness. Large powder particles induce higher surface roughness as compared to thinner counterparts [37]. The as-built surfaces of several rectangular and cylindrical samples were characterized using ALICONA FOCUS XL optical roughness system. For each tray, the roughness was studied on 3 bending specimens (2 measurements per specimen corresponding to 2 faces) and 3 torsion specimens (1 measurement per specimen). Surface and linear roughness parameters were measured according to ISO 25178 (for surface roughness) and the ISO 4287 (for linear roughness) standards. Examples of measured surface and line roughness for bending and torsion samples are shown in Fig. 3. The mean values of measured parameters are provided for each tray in Table 3. Generally, the cylindrical samples have rougher surfaces than the rectangular ones. But the differences are not significant.

2.2.3. Porosity

µCT tomography was performed on several samples of 4 mm diameter and 10 mm length. Fig. 4a shows the image of a section distant from the edge in the Z plane, Fig. 4b shows the superposing of all sections and Fig. 4c illustrated the 3D size (in pixel) and distribution of defects. The device capacity, the sample size, and the acquisition parameters make it possible to view the defects greater than 8 µm (corresponding to the size of one pixel). For all the samples, the defects have an equivalent diameter of fewer than 7 pixels (about 50 µm) and they are distributed randomly in the volume. Quantitative analysis showed that all the measured samples have a very good density that exceeds 99.95%. The maximum porosity rate measured was less than 0.04%. µCT is not intuitive to exhibit the morphology of the internal defects due to the limitation of pixel definition. A destructive analysis (cutting and polishing) was carried out to better present those volume defects. From SEM images (Fig. 5), three types of internal defects are presented: a

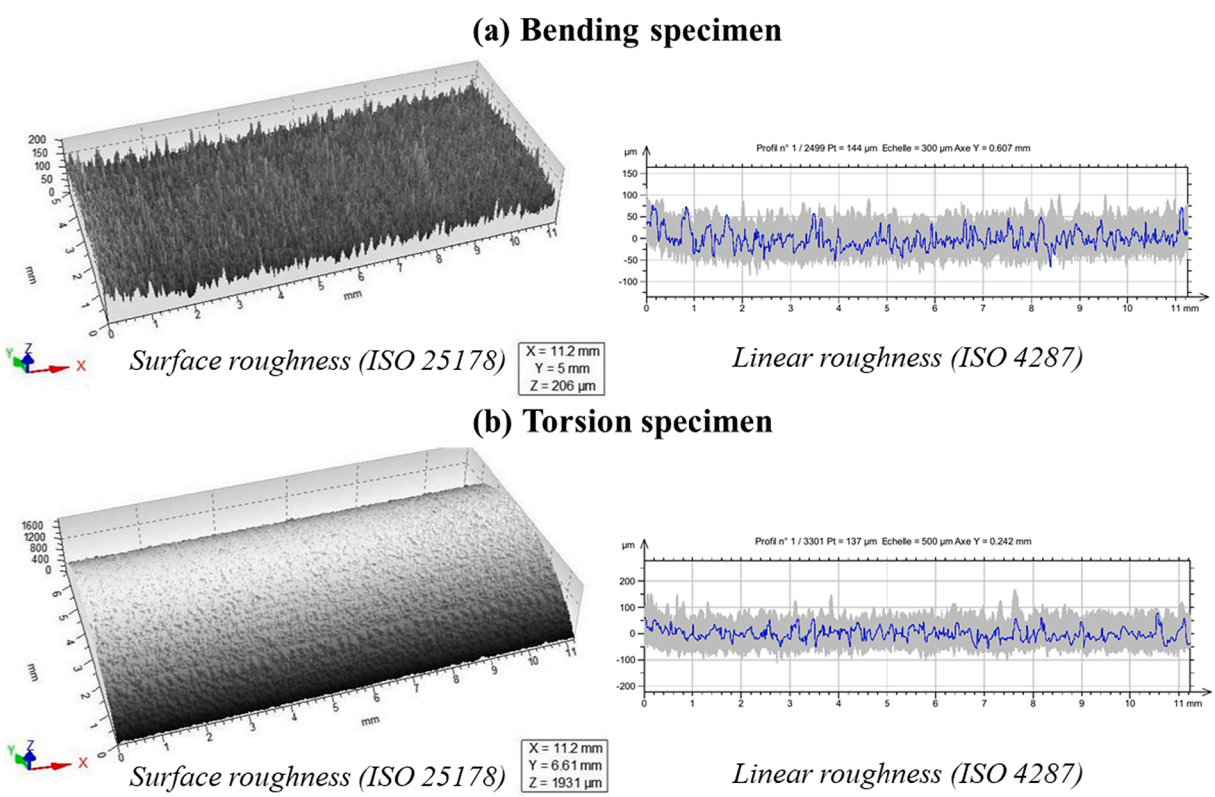

Fig. 3. Surface and linear roughness in (a) bending specimen and (b) torsion specimen.

Table 3
Mean values of surface and linear roughness parameters.

Specimens	Sa [µm]	Sq [µm]	Sz [µm]	Ra [µm]	Rq [µm]	Rz [µm]
Bending Tray 1	11.3 ± 2.2	14.7 ± 2.8	139.3 ± 28.1	10.6 ± 2.4	13.7 ± 3.1	76.5 ± 17
Bending Tray 2	11.2 ± 2.1	14.8 ± 3.1	147.7 ± 17.5	10.8 ± 1.9	13.9 ± 2.4	77.4 ± 14
Torsion Tray 1	12.6 ± 2.4	16.2 ± 2.7	154 ± 17.8	13.4 ± 0.2	17.1 ± 0.1	93.5 ± 3.2
Torsion Tray 2	11.2 ± 1.2	14.4 ± 1.4	142 ± 14.8	13.6 ± 1.1	17.3 ± 1.1	92.2 ± 3.6

Ra: Arithmetical mean height of the profile — *Sa: Arithmetical mean height of the surface*
Rq: Root mean square height of the profile — *Sq: Root mean square height of the surface*
Rz: Maximum height of the profile — *Sz: Maximum height of the surface*

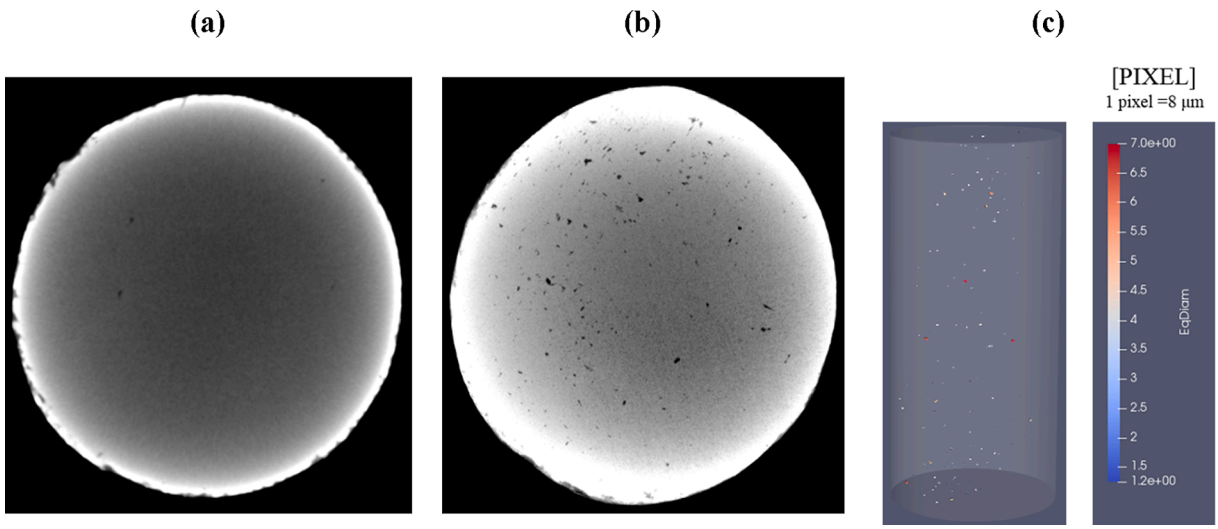

Fig. 4. Tomography in Z-plane: (a) slice No.250, (b) superimposing all slices and (c) 3D size and spatial distribution of the detected defects.

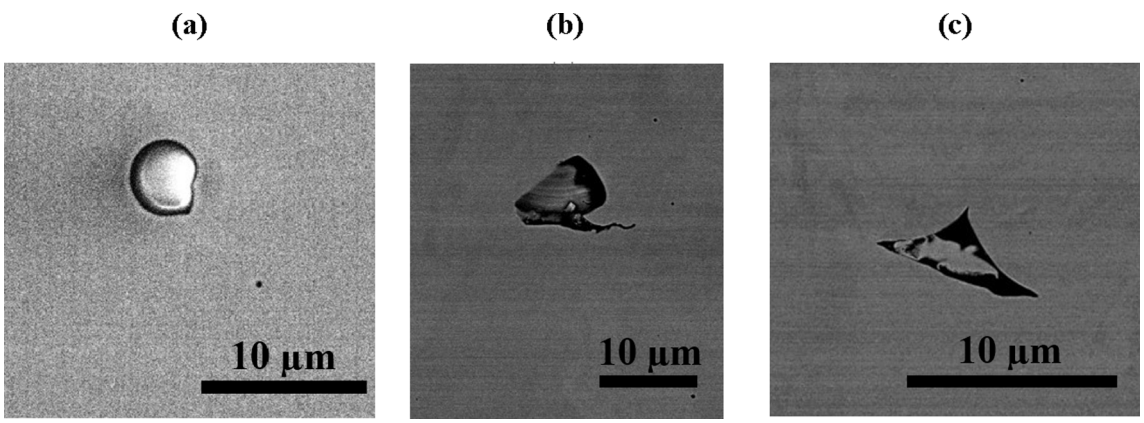

Fig. 5. Process-induced defects observed under SEM: (a) un-melted powder, (b) lack of powder, and (c) pore formed between the particles of powder.

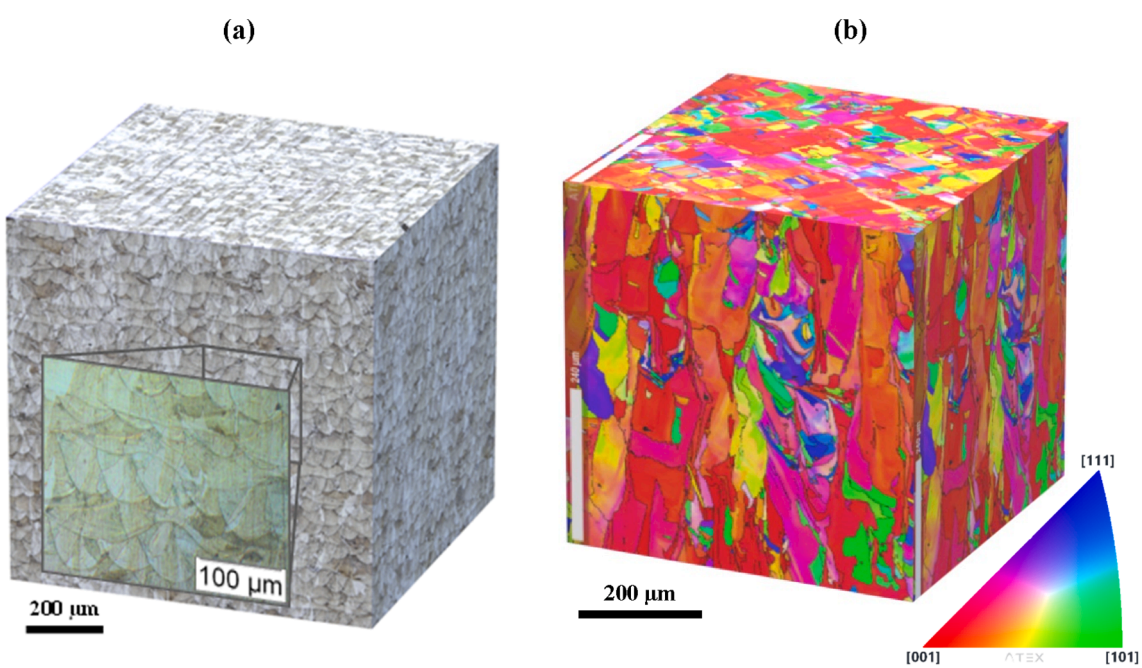

Fig. 6. (a) 3D microstructure of the LPBF 316L SS observed by (a) optical microscopy (×100 and ×250) and (b) SEM- EBSD (the building direction was vertical).

particle of un-melted powder; a lack of powder; a pore formed between the particles of powder. SEM observations on the core of the samples confirmed that the fabricated material has very few internal defects.

2.2.4. Microstructure

The microstructure can be seen in Fig. 6a. The building direction was vertical. It is possible to distinguish ellipses, characteristic of the LPBF process since they represent a section of the melt pools which appear during the passage of the laser. The macrostructure resembles fish scales. We can see also the elongated shape of austenitic grains crossing several layers. We can also observe the grains that are formed during the manufacturing process. Their growth direction roughly coincides with the vertical axis of the specimen. The grains are columnar, pass through the melt pools, and consist of dendrites resulting from rapid solidification after the laser passage. The electron backscatter diffraction (EBSD) was also used to analyze the grain morphology and orientation as seen in Fig. 6b. The grain size is not homogeneous. Elongated columnar grains that cross several layers are visible and there are no twinning boundaries in these maps. $\langle 001 \rangle$ texture is illustrated by the EBSD orientation maps.

3. Fatigue tests

3.1. Experimental fatigue test set-ups and conditions

The fatigue tests aim to better understand the effects of the surface states and the loading modes. The tensile fatigue tests were conducted in ambient air and temperature on a biaxial servo-hydraulic testing system, MTS® 809. The experiments were carried out under stress control at a load ratio $R = -1$ and a frequency of 15 Hz. A table resonant testing machine, Rumul® CrackTronic, was used to carry out the bending and torsion tests. The test frequency was not controlled but depends on the specimen stiffness. In the current study, the values of the frequency reached were $f = 96–98$ Hz for the as-built specimens and $f = 94–96$ Hz for the polished specimens. Temperature was always measured by the thermocouple during all the tests. No evident heating was observed. The threshold of "run-out" in all the three loading configurations was set to $2 * 10^6$ cycles.

The fatigue behavior of metallic components is greatly dependent upon the surface state. Nevertheless, machining, which is usually applied to eliminate surface irregularities in the literature, is not used in this study because machining AM components of complex shapes is not always achievable. We tried, as far as possible, to avoid the introduction of local plastic deformation and residual stresses at the surface. Hence, mechanical polishing is expected to be the most adapted technique to remove surface irregularities. Three different surface state conditions were hence investigated: as-built (AB), simple-polished (SP), and total-polished (TP). Surface treatment is conducted via polishing with grit sandpapers from 120# to 2400#. The resulting surface roughness is expected less than 1 μm (Ra). For the SP case, we removed only the surface roughness on the free surface. The thickness of the removed layer is approximately 50 μm. For the TP case, we polished the whole surface of the specimen to remove the surface roughness. Then, we continued the polishing until a layer of about 250 μm thickness was removed. To recall that the contouring step was intentionally skipped during the fabrication process, the TP samples actually remove the contour zone if contouring has been conducted. A batch of wrought machined 316L bending samples sharing the same dimension with the AM 316L samples were also prepared for comparison purposes.

3.2. Fatigue strength results and analysis

The S-N curves for the three loading modes and the three surface state conditions are shown in Fig. 7. The average fatigue strengths calculated by the staircase method are listed in Table 4.

Surface treatment improves fatigue performance, and the improvement is more pronounced under tension or bending than under torsion. In the tension loading condition, two sets of specimens are used to study the effect of surface roughness: as-built specimens and simple-polished specimens. Simple-polishing increases the average fatigue strength from 92.5 MPa to 115 MPa, i.e., a 24% increase. Likewise, fatigue tests under bending loading show a 29% increase in the fatigue strength for simple-polished specimens compared to the as-built specimens. Results from the torsion loading are slightly different. The as-built specimens show an average fatigue strength of 127 MPa while the simple-polished results lead to a value of 143 MPa. The difference is thus 12% and is apparently lower than the one from the other two loading modes. Hence, eliminating the surface roughness may improve the fatigue strength of LPBF SS 316L. For the bending and torsion fatigue tests, besides the AB and SP specimens, a set of TP specimens is added. The difference observed between the SP specimens and the TP specimens may reflect the effect of the omitted contouring procedure. The fatigue strength has been further improved after the additional polishing. The bending samples have a fatigue strength of about 138 MPa after total-polishing, which is 53% higher compared to that of SP samples. Total-polishing promotes the torsion samples having a fatigue strength of 172 MPa. But the increase from total-polishing compared to simple-polishing is 35% for torsion which is not as significant as that for bending.

No evident difference was found between the tension and bending fatigue tests. Previous research often reports that the bending fatigue strength is higher than the tension fatigue strength due to the beneficial stress gradient effect [38]. In the present study, the fatigue strengths under tension and bending are both remarkably lower than the common strength of wrought 316L. In this regard, the stress gradient effect was not detected and might be masked by other phenomena. The experimental investigation also reveals that the LPBF SS 316L has a higher average fatigue strength under torsion than under bending or tension. This observation should be put in perspective, as our fatigue data are highly scattered and the number of tests per condition is maybe not enough. That being said, if we assume that the average fatigue strengths under torsion and tension are close, it does mean that the alloy shows a brittle type behavior, as alloys containing defects (cast iron, cast aluminum alloys …) most of the time do [39,40]. The fractographic observations should help explain this macroscopic behavior.

Regarding LPBF 316L, the defects may degrade the material in terms of its HCF behavior. But the effect of defects in different loading modes needs to be assessed. Different relative strengths under bending/tension or torsion loadings of the samples following the same fabrication and post-treatment protocol are noted. For the TP torsional samples, the fatigue strength obtained is about 172 MPa which is in fact similar to the data reported in the literature for machined LPBF 316L as shown in Fig. 7(d) [31]. And, it is slightly higher than the value of 148 MPa from torsion fatigue tests for the wrought machined 316L in the reference [28]. Before an in-depth analysis, an easy way to have the estimate of fatigue strength is presented in Eq. (1) [41].

$$\sigma_w = (0.4 \sim 0.5)\sigma_b \tag{1}$$

In which σ_w denotes the uniaxial fatigue limit and σ_b denotes the tensile strength. The tensile strength of the studied material is about 610 MPa. Thus, the uniaxial fatigue strength should be about 246–305 MPa.

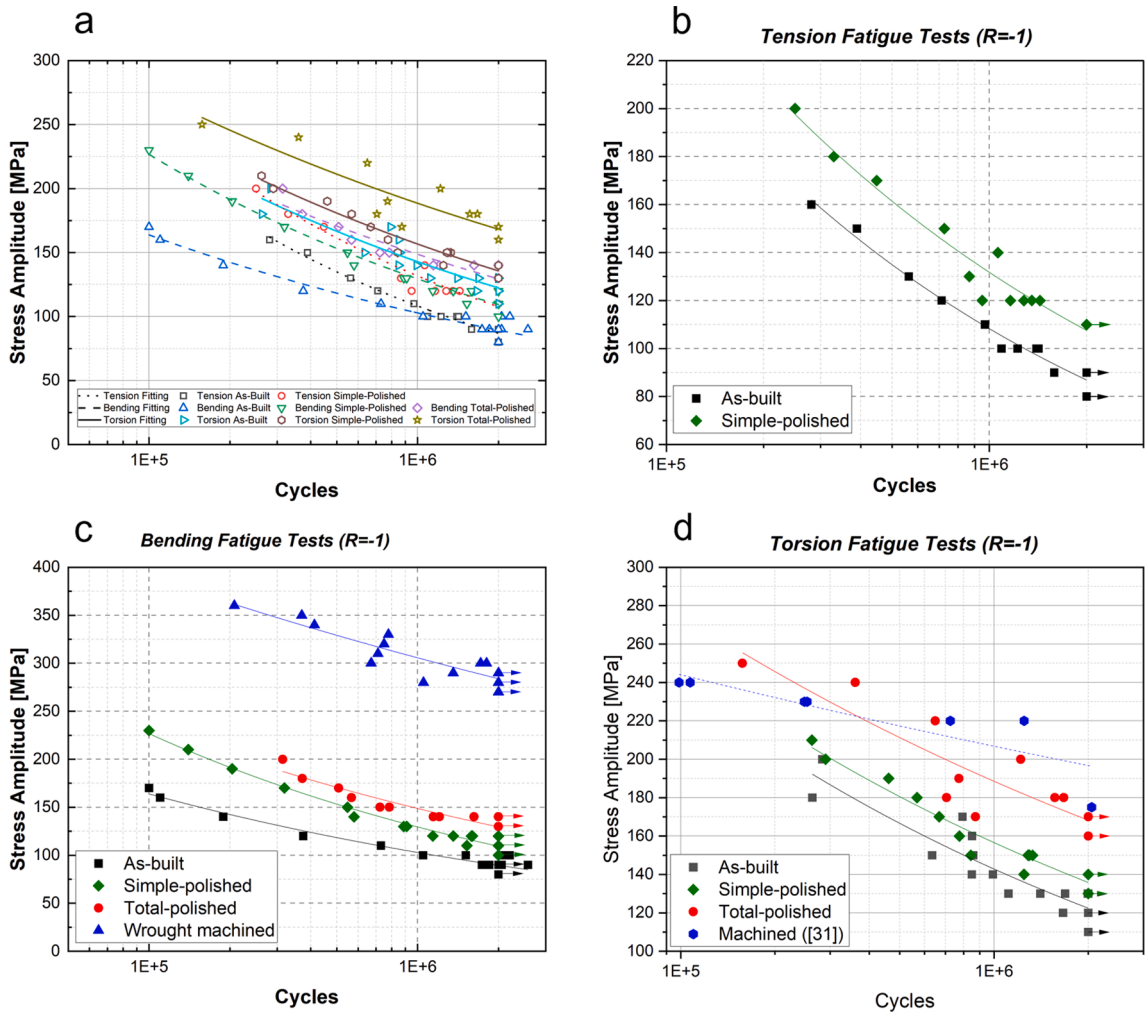

Fig. 7. S-N curves for different surface state conditions in different fully reversed loading modes: (a) summary plots; (b) tension–compression; (c) plane bending; The fatigue test results for machined specimens of wrought 316L steel are also given for comparison; (d) torsion; with reference from [31].

Table 4
Fatigue strength values at 2 * 10^6 cycles assessed with the staircase method for different surface state conditions and different loading modes.

Surface finish	Loading condition		
	Tension	Bending	Torsion
As-built	**92.5**	**90**	**127**
Simple-polished	**115** (24% ↑)	**116** (29% ↑)	**143** (12% ↑)
Total-polished	–	**138** (53% ↑)	**172** (35% ↑)
Unit: MPa			

By adapting the von Mises criterion, the equivalent stress of the torsional fatigue loading for TP torsion samples is about 295 MPa which is actually $\sqrt{3}$ times the actual torsional stress amplitude. However, for TP bending samples, the fatigue strength is only 138 MPa. The empirical estimate is effective to predict torsional fatigue limit but not bending. That is to say, the torsional samples outperformed the bending/tension samples under cyclic loadings despite they were fabricated simultaneously. The reason behind that might be because the size and shape of defects affect the fatigue behavior differently in various loading modes.

To understand the origin of the differences among the results from the different batches, a better knowledge of the failure mechanisms occurring in different surface-treated specimens and under different loadings is essential. Hence, the fractographic analyses are carried out and detailed in the next section.

4. Fatigue fracture mechanisms

Fractographic analysis was conducted to explore the mechanism of fatigue failure in LPBF 316L. All bending specimens and torsion specimens were inspected. Tension specimens were not exploitable because the fracture surfaces were damaged during the stress-controlled cyclic tension–compression loading of R = −1.

4.1. Bending samples

Concerning the TP specimens, the fracture surfaces show similar features. In general, a large cowrie pattern area with river shape fatigue striations emerging from one or two points can be seen. The fatigue crack initiation sites are always located on the free surface. Regarding the position(s) of crack initiation(s), there exist two kinds of situations: single site and multiple sites (mostly 2 sites, in this study). In terms of the situation of crack initiation, 2 categories are used: single defect at initiation site and several adjacent defects at initiation sites, as shown in Fig. 8. Among all the defects observed, two representative defect shapes can be distinguished. Most of the time, the observed defect presents a semi-elliptical shape while irregular shapes can be seen occasionally. The elongated defect can be considered approximately as an ellipse with an ellipticity ratio of about 3 to 5. It is always the major axis of the elliptical defect that penetrates the solid part. Hence, the defect is even more harmful under the perpendicular loading and leads to a strong stress concentration as well as a strong stress gradient.

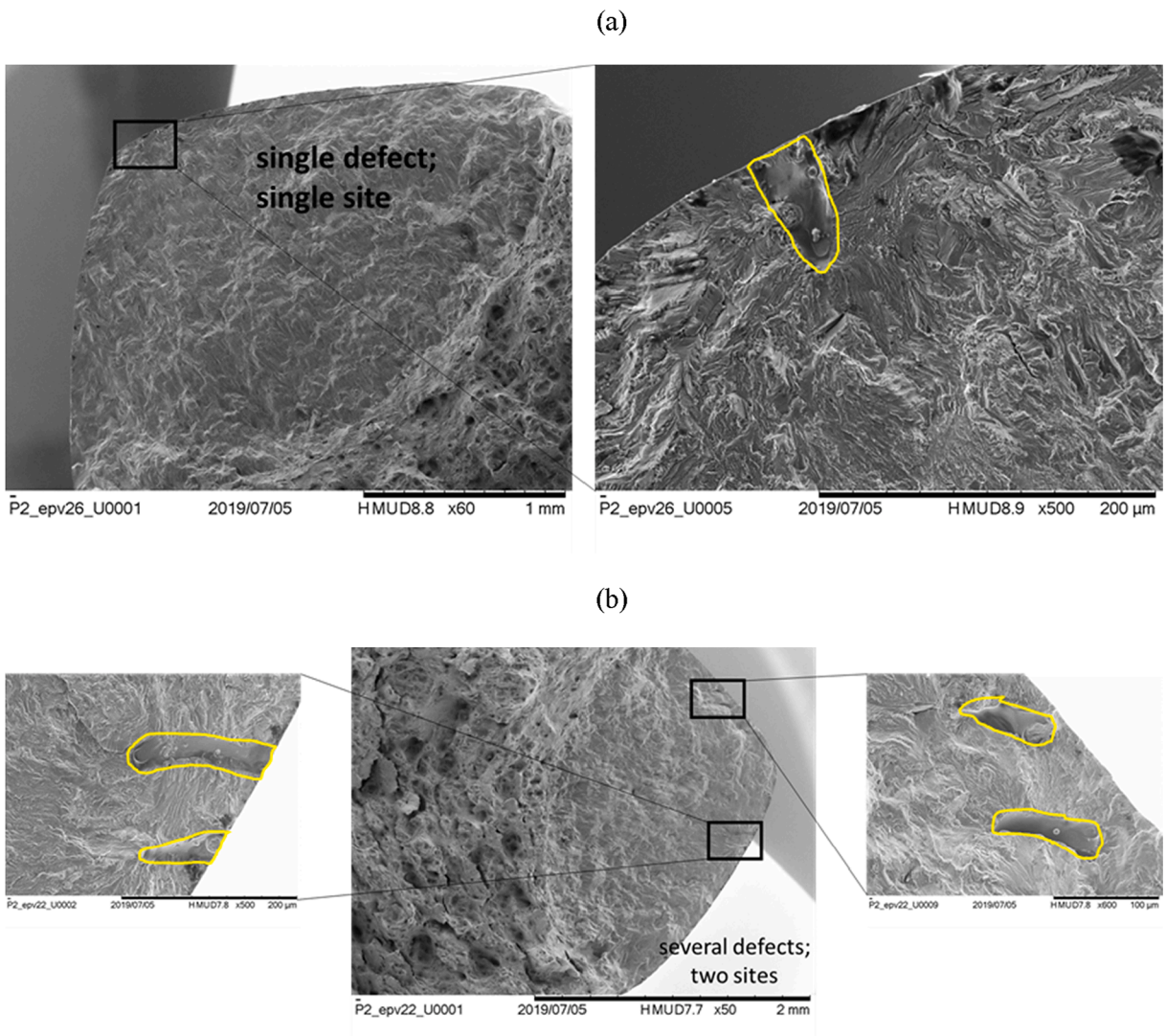

Fig. 8. SEM observations on fatigue crack initiation site(s) in total-polished LPBF 316L bending specimens: (a) single defect at one initiation site (Tray2-S26); (b) several defects at two initiation sites (Tray2-S22). Elongated-shaped defects can be seen.

About SP specimens, unlike the total-polished specimens, several cracks in one specimen can be observed. 9 out of 13 specimens present only one fatigue crack while the remaining 4 specimens present clearly 2 independent fatigue cracks. A representative picture for 2 independent fatigue cracks in one specimen is shown in Fig. 9(a). In the above discussion about total-polished specimens, we mention a configuration that a fatigue crack can possibly initiate from several sites. There is a possibility that all the initial defects contribute to the crack formation while it is also possible that the subsidiary defects can only cause non-propagated cracks and later the cracks are activated due to principal defects. But it is clear that the multiple cracks form solely and do not interact with each other. Even without the presence of other cracks, one crack can lead to fatigue failure.

Another difference between simple-polished specimens and total-polished specimens is that the presence of defects increases significantly. As shown in Fig. 9(b and c), several parallel adjacent defects with similar morphology are seen. The shape of the defect is close to the defect observed in the total-polished specimen. It is expected that this defect is due to the fabrication process. Compared to other research in which the contouring step is usually included, this pattern of defects arrangement is never reported, even for as-built products. The clusters of LoF defects play the predominant role compared to the lateral surface roughness in those cases. In the total-polished specimens, we observed adjacent LoF defects but not as clustered as those of the simple-polished specimens. The explanation can be that those LoF defect clusters exist mostly on or near the surfaces. This finding complements the research concerning the effect of contouring. Koutiri et al. investigated the SLM (LPBF) process parameters on the surface finish, porosity rate, and fatigue behavior by a combined hatching + contouring procedure [42]. Process optimization is thus often a compromise between an optimum densification state and a minimum number of contaminating spatters. An optimized contouring procedure can notably reduce the pores near the surface [19]. However, defects remain in the transition zone between the hatching and the contouring. The additional problematic is that the contouring zone usually cannot be preserved during machining if the as-built surface is needed to be treated. In this study, we can

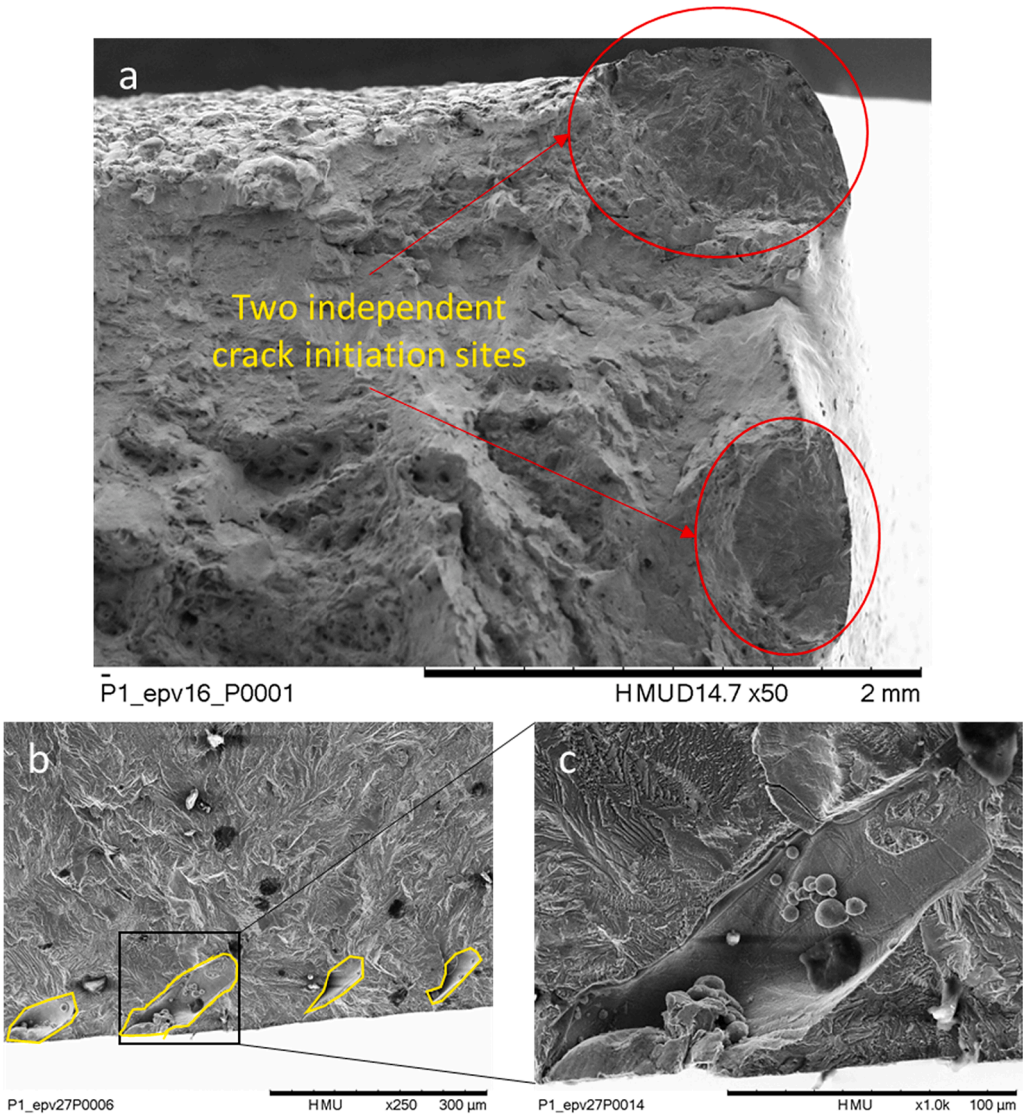

Fig. 9. SEM observations on fatigue crack initiation site(s) in simple-polished LPBF 316L bending specimens: (a) two independent fatigue crack initiation sites in the specimen (Tray1-S16); (b) parallel adjacent defects at one crack initiation site and (c) a zoomed view of one LoF defect (Tary1-S27).

remove a thick layer of material on the outer circumference by grinding, thereby reducing the effect of subsurface LoF defects due to the imperfection of hatching process. But, for a complex-shaped component in which the hatching process parameters and the contouring process parameters are not ideally matched, or the contouring process is not applied, the pattern of LoF defects' distribution at the subsurface should be consistent with the observation on the SP samples in the current study.

The as-built specimens keep all inherent defects. The photos (Fig. 10) typically show the main mechanism of fatigue failure for as-built specimens. Several defects are found in the vicinity of the initiation site. Those defects acting simultaneously or successively are responsible for the fatigue failure. A series of parallel defects distributed on the top surface is seen in Fig. 10(a). In Fig. 10(b), in the edge of the specimen, both roughness defects and lack-of-fusion pores make the surface state extremely poor. In terms of morphology, the defects found in the as-built specimens are often the inclined elongated LoF defect. The defects are often a combination of lack-of-fusion and surface imperfection which is caused by surface tension or precision of laser projection. For the defect as shown in Fig. 10(c), its open-form makes it detectable under profilometry, while in Fig. 10(d), the defect is subsurface and cannot be measured by a surface scan.

The LoF defect is usually flat and undetectable under µCT. The elongated morphology plus the deep penetration of LoF defect are very harmful in terms of fatigue. For the as-built specimen, LoF defects combined with surface roughness strongly decrease fatigue performance. Simple-polishing which removes a thin layer of the surface can only get rid of roughness. A cluster of adjacent LoF defects can still be seen. Nevertheless, a stronger polishing removing a layer of 250 µm seems to be insufficient to eliminate all the LoF defects. The LoF defects at the crack initiation site seem though fewer in total-polished specimens. We can deduce that the distribution of LoF defects is highly concentrated on the surface. Under a certain depth, the presence of the LoF defect decreases. For most of the total-polished specimens, we can

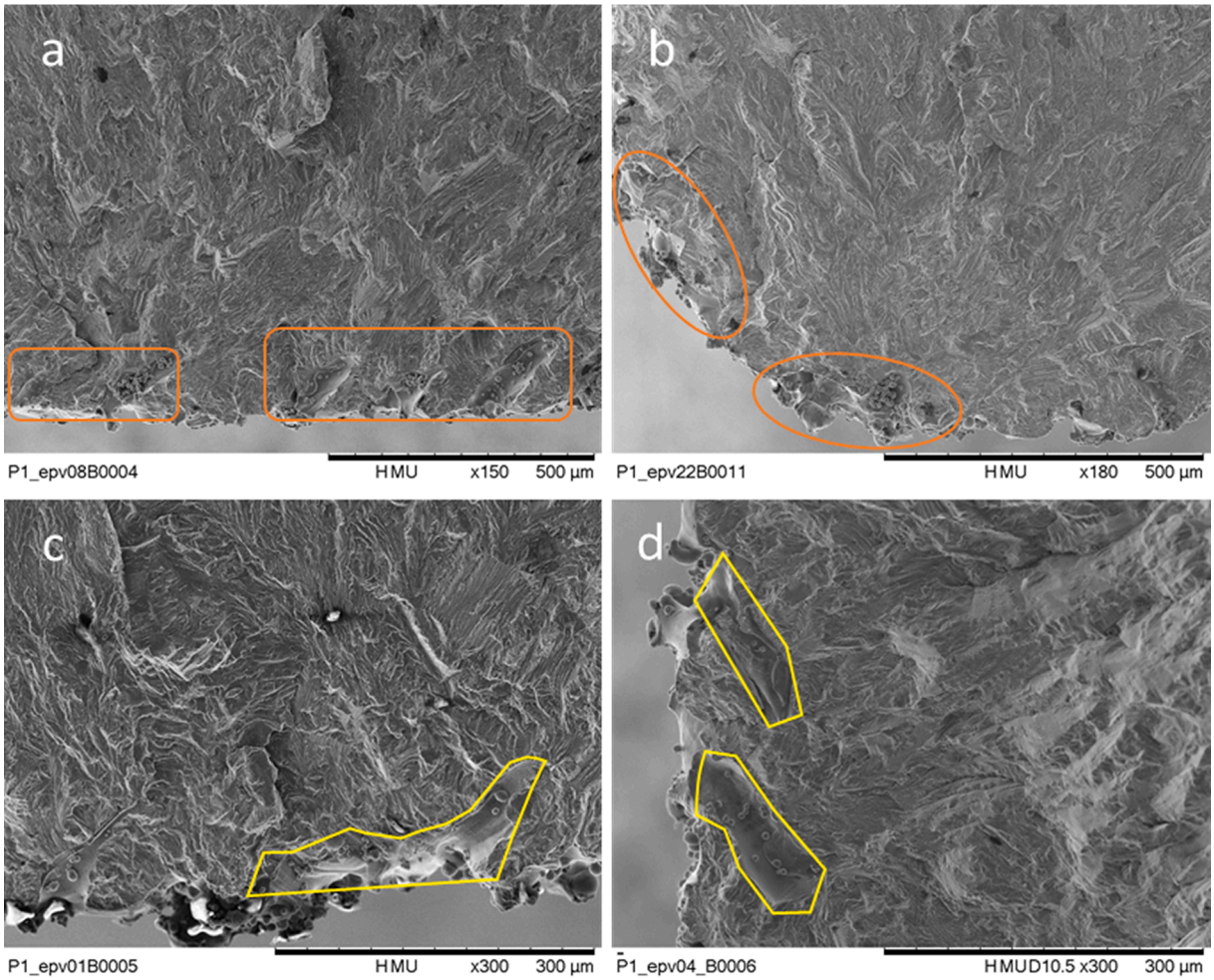

Fig. 10. SEM observations on fatigue crack initiation site(s) in as-built LPBF 316L bending specimens: representative crack initiation sites (a) in the middle of the top surface and (b) in the edge of top surface; typical presences of defects: (c) open defect due to roughness and LoF; (d) subsurface defect from LoF.

Table 5
Summary of fractography observations on all the bending samples.

Specimen number		Total polished		Simple polished		As-built	
		10		14		15	
Fatigue failure/(undefined type failure)		10/(0)		13/(1)		13/(2)	
Single crack	Multiple cracks*	10	None	9	4(2)	11	2(2)
Fatigue crack observed		10		17		15	
As-built surface	Polished surface	None	10	13	4	15	None
Single site	Multiple sites†	8	2(2)	15	2(2)	Uncountable	
Initiation site		12		19			
Single defect	Adjacent defects#	6	5(2);1(3)	11	3(2);1(3);1(4);1(5);1(8)		
Inherent defect observed		19		36			
Elongated defect	Irregular defect	15	4	19	17		

Note: *: Number of specimens with multiple cracks (number of cracks).
†: Number of cracks having multiple sites (number of sites).
#: Number of sites having adjacent defects (number of defects).

find only one unique fatigue crack while multi-cracks are observed for as-built and simple-polished specimens. All the initiation sites are found on the surface or subsurface. The above-mentioned observations are summarized in Table 5.

4.2. Torsion samples

In the classical fracture mechanics theory, the propagation of crack is categorized by three modes: opening mode, sliding mode, and tearing mode. A typical torsion fracture mechanism is that after initiation, a mode II crack growth is observed in the first stage. The crack path is on the plane of maximum shear stress. From a critical crack length, the crack path changes, and mode I becomes predominant (stage II). The crack propagates in two perpendicular planes experiencing the maximum normal stress. Regarding AM materials, very few results are reported in the literature about the fatigue crack growth features under torsion loading. To the authors' best knowledge, there is no result of the as-built LPBF 316L. The aim of the present investigation on torsion

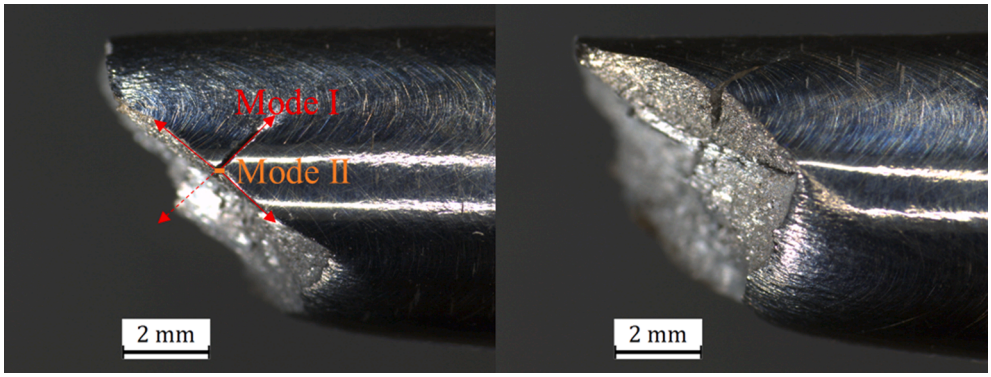

Fig. 11. Macroscopic crack path in total-polished torsion specimen: stage I (mode II) followed by stage II (mode I).

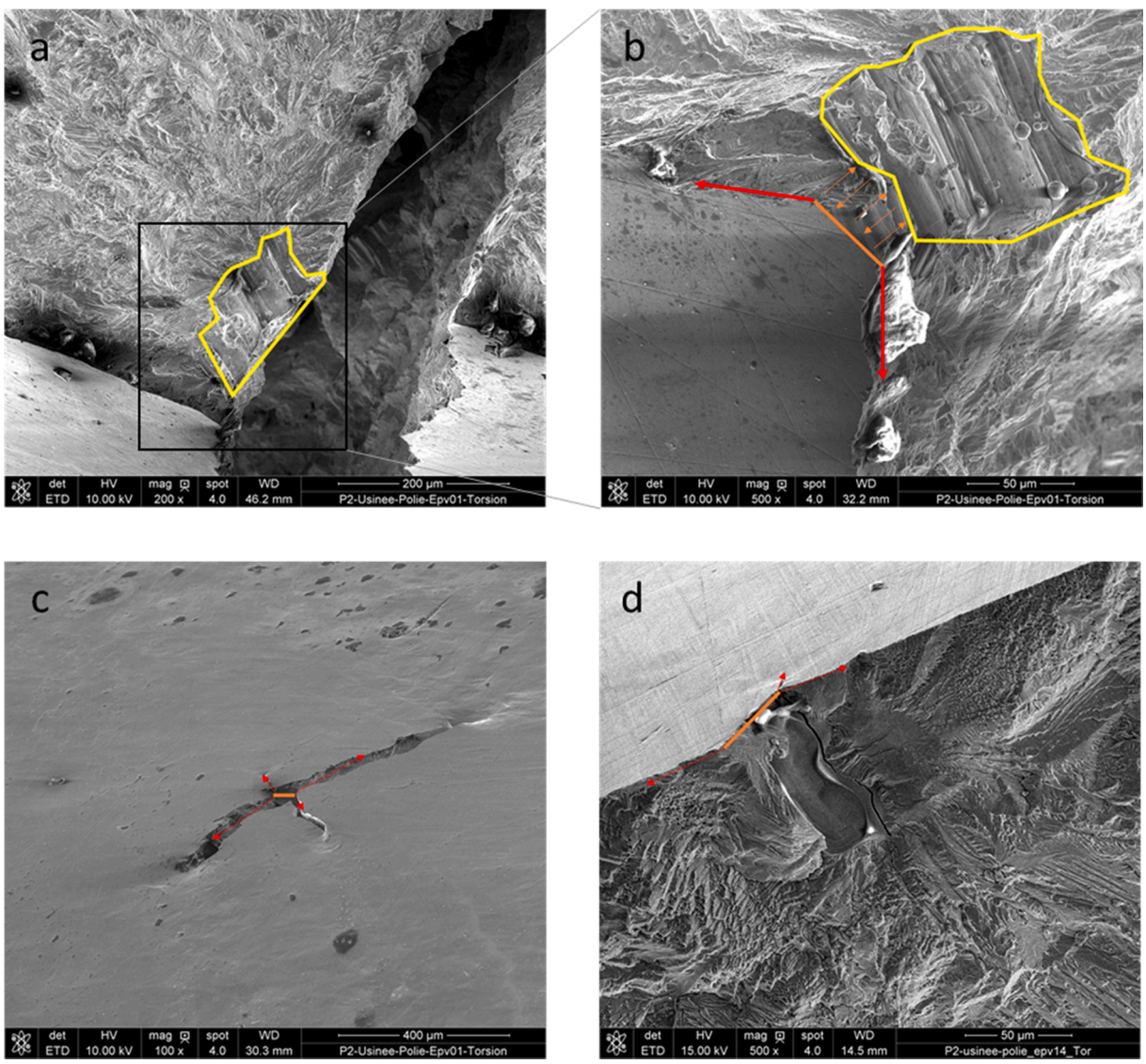

Fig. 12. SEM observations of total-polished LPBF 316L torsion specimens: (a and b) fracture surfaces and (c) secondary crack of one same specimen; (d) example of the fatigue crack initiation and growth mechanism from defect under torsional loading, two stages are visible.

fracture surfaces is to clearly explain the role of defects on crack initiation and growth and to check if stage I (mode II) and stage II (mode I) are observed.

Some observations on the free surface of the gauge length are conducted for the total-polished specimens after failure. It can be seen that the specimen breaks into two parts because of mode I crack perpendicular to the maximum normal stress planes. The normal direction to the fracture surface and the axial direction of the specimen makes a 45° angle. Besides the two cracks which go through the entire section, one smaller crack oriented 90° to the specimen axis is visible in the central

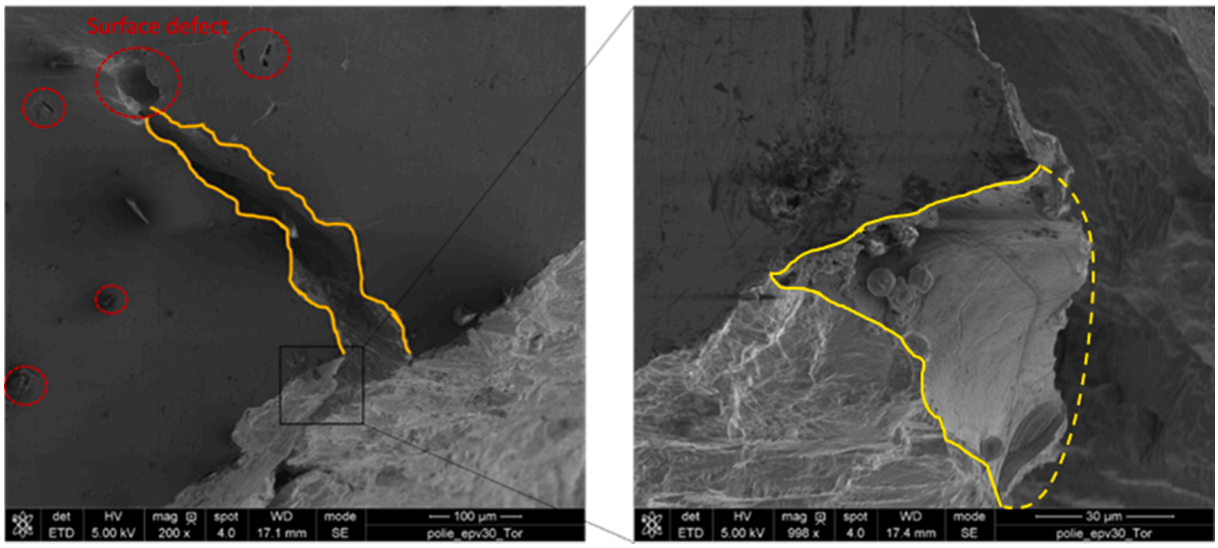

Fig. 13. Fracture surface observation on the simple-polished LPBF 316L torsion specimen.

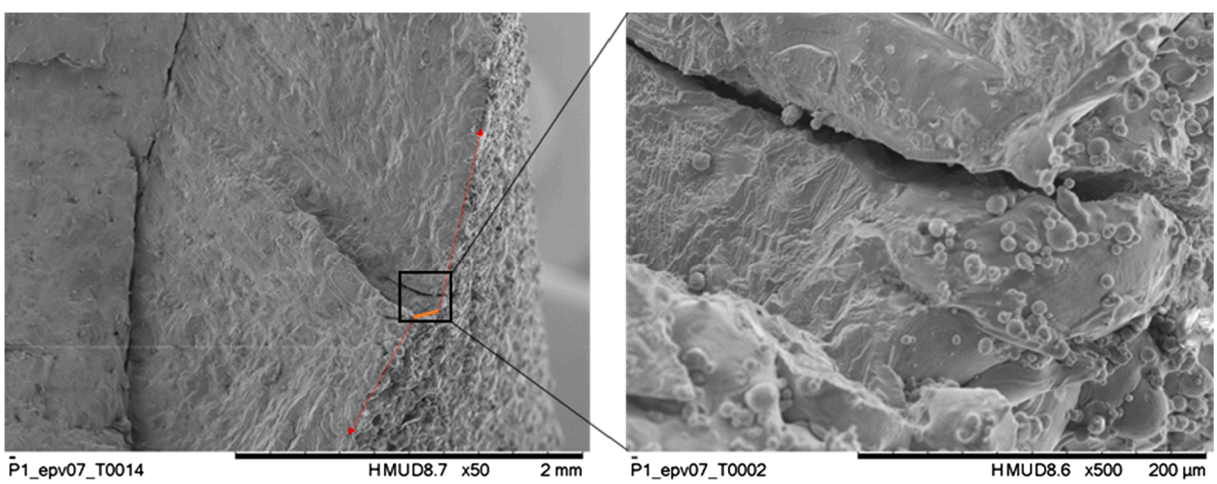

Fig. 14. Crack path and defects at the origin of failure in an as-built LPBF 316L torsion specimen.

initiation area. It is then clear that the observed mode I crack originates from a mode II crack as can be seen in Fig. 11. As the mode II crack is small, SEM observations are carried out to better illustrate the first stage of crack initiation and propagation.

From Fig. 12(a and b), we can see that an LoF defect is responsible for the crack initiation. This defect lies in the subsurface of the specimen and is not eliminated by polishing. Two perpendicular cracks form from both sides of the defect. The size of this LoF defect is similar to that in the bending specimens. A photo from the same specimen of a secondary crack is shown in Fig. 12(c). It is observed that crack initiates in shear mode and expands along the maximum normal stress planes. As mentioned before, the polishing procedure completely removes the surface roughness. But surface defects, in particular, LoF defects, are still present. For the great majority of total-polished specimens, the LoF defect can be found at the initiation site of fatigue crack (see Fig. 12(d)). The crack path is seen clearly on the free surface. The shift from the shear stress plane to the normal stress plane confirms the proposed fatigue failure mechanism.

The crack path in the simple-polished specimen is not as typical as the one in the total-polished specimen. Generally, the main crack still follows the maximum normal stress plane. The presence of surface defects seems to affect the crack propagation path. The local stress concentration can hence result in a change of maximum normal stress plane orientation and lead to a tortuous crack path (see Fig. 13). A zoom view at the crack initiation site exhibited that an LoF defect triggered the crack initiation and was torn apart during the propagation.

As for as-built specimens, the normal to the fracture plane is oriented 45° to the specimen axis, meaning the mode I crack is still predominant in Stage II. But the non-coplanar fracture surfaces indicated the existence of the mode II horizontal crack. And it should be stressed that an obvious staircase-like transition zone (denoted by the orange line in Fig. 14(a)) between the two 45°-inclined fracture surfaces was seen. Besides, near the transition zone, a secondary Mode II crack was also seen. These are the direct proof that even if the AB samples have a very poor surface state and the surface is almost covered with defects, Mode II still plays the dominant role in Stage I. Concerning the inherent defects, a series of large LoF defects was at the initiation site (see Fig. 14(b)). The horizontal mode II crack grows among adjacent LoF defects. The critical defect's presence was much more frequent compared to each of the polished specimens. Moreover, the size of the defect was larger, and neighboring defects were often seen.

5. Influence of the defects on fatigue strength

In the HCF tests presented in Section 3, it is mentioned that the samples have poor fatigue strengths which are usually because of the

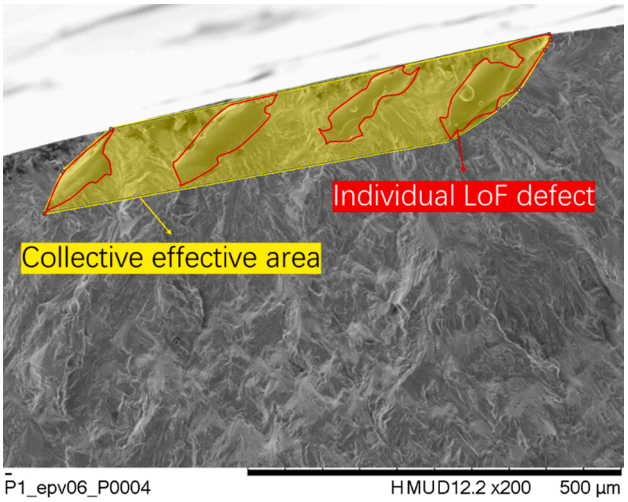

Fig. 15. Two measurement techniques to assess the size of a cluster of adjacent defects: consider only the largest defect and treat all defects as one.

presence of defects. The fractography observations confirmed the assumption. Almost all fatigue cracks are initiated from the intrinsic LoF defects. The defects are flat with often an elongated shape. Moreover, at the crack initiation sites, a number of defects are always seen, which is particularly obvious in the AB and SP samples. And even in half of the TP samples, there are also multiple gathering defects seen. These clusters of adjacent sharp defects are likely to be very detrimental to the fatigue strength and could explain the differences in measured fatigue strengths with the literature data.

The irregular shape of the LoF defect makes it difficult to choose a representative parameter to describe its geometry. There are investigations about the fatigue performances and LoF defects in AM materials in literature [39,43,44]. But the enumerated studies focused more on how to quantify the size of one irregular defect whilst few have discussed the case where a series of defects clusters at one site. Houria [45] proposed a way to consider two defects at one crack initiation site. If the two defects are close to each other, they are treated as one big defect. Therefore, we use two assumptions, one is to consider only the largest single defect at the crack initiation site in which the largest defect solely triggers the crack initiation; the other one is to treat each of the defects observed at the crack initiation site as one large defect. Examples are shown in Fig. 15. For both of the two methods, we use $\sqrt{area}$ to describe the size of defect. The samples in different surface conditions are measured, the averages and standard deviations are listed in Table 6. An equation (Eq. (2)) is often used to predict material's bending fatigue strength based on the measured defect size ($\sqrt{area}$) and the hardness (Hv). Predictions are also listed in Table 6. It is not very surprising that the equation does not yield good predictions for the LPBF 316L, because it is based on the empirical relationship (Eq. (3)) between the threshold stress intensity range (ΔK_{th}) and defect size as well as the hardness derived from experiments of a series of wrought steels. Even though the predictions are not satisfying because the empirical values cannot fully reflect the AM material's behavior, it is worth noting that treating the clustering defects as one seems to be a good idea as it describes better the influences of the defects on fatigue strength (see Table 6).

$$\sigma_w = \frac{1.43(Hv + 120)}{\left(\sqrt{area}\right)^{\frac{1}{6}}} \tag{2}$$

$$\Delta K_{th} = 3.3 \times 10^{-3}(Hv + 120)\left(\sqrt{area}\right)^{\frac{1}{3}} \tag{3}$$

Another noteworthy finding is that the bending fatigue strength is lower than the torsional fatigue strength. Endo and Yanase have revealed that torsional fatigue strength is related to the threshold

Table 6
Bending fatigue strengths in experiments and measured defect sizes with the corresponding fatigue strength predictions (hardness of the studied LPBF 316L is 226 Hv).

Type	$\sigma_{w,\ Exp}$ [MPa]	Defect size (Single) [µm]	$\sigma_{w,\ prediction}$ (Single) [MPa]	Defect size (Multiple) [µm]	$\sigma_{w,\ prediction}$ (Multiple) [MPa]
As-built	90	117 ± 23	217–232	408 ± 99	175–190
Simple-polished	116 (29%↑)	112 ± 34	216–239 (0.7%↑)	176 ± 60	199–224 (15%↑)
Total-polished	138 (53%↑)	74 ± 16	234–251 (8%↑)	101 ± 29	220–242 (26%↑)

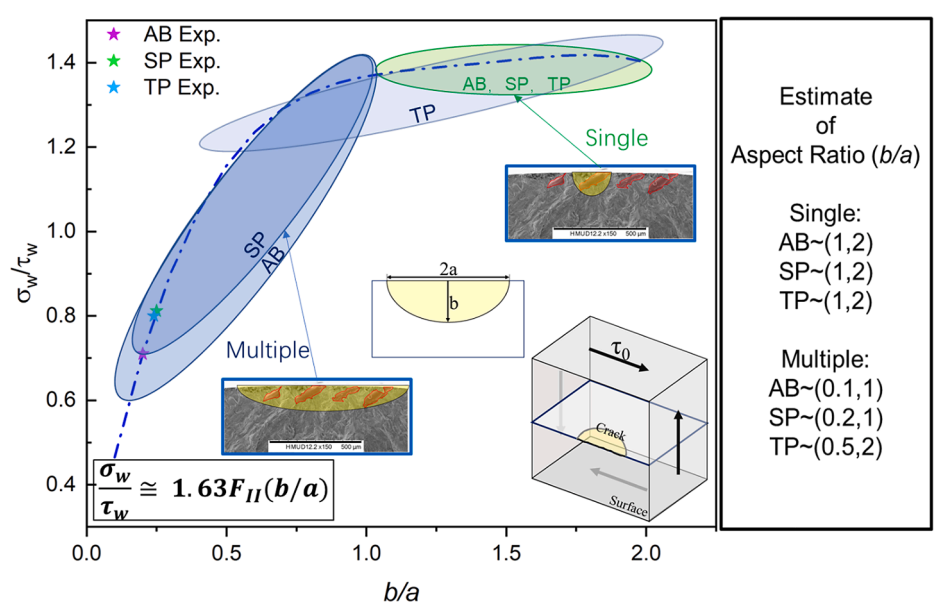

Fig. 16. A plot of the relationship between aspect ratio (b/a) and fatigue strength ratio (σ_w/τ_w). In the plot, the two different measurement methods are schematically presented to give estimates for the aspect ratio. The fatigue strength ratios from experimental results are shown for reference.

condition for continuous propagation of a macroscopic Mode I branched crack [46]. The sample containing a crack subjected to torsional loading can be equivalently converted to a sample subjected to bi-axial tension and compression loading [47]. The relations between maximum stress intensity factor and the crack sizes under bending and torsion loading respectively are presented in Eqs. (4) and (5), in which σ_0 denotes the remote tensile stress, τ_0 denotes the remote shear stress, F_{II} is a geometrical factor formulated by the aspect ratio (b/a).

$$K_{I,max} \cong 0.65\sigma_0\sqrt{\pi\sqrt{area}}(surfacecrack) \tag{4}$$

$$K_{II,max} \cong F_{II}\tau_0\sqrt{\pi\sqrt{area_p}} \tag{5}$$

Because the fracture surfaces of the torsional fatigue sample are always inclined under SEM observations, it is difficult to accurately measure the defects. Considering that the crack-initiating defects in both bending and torsional samples are essentially the same intrinsic LoF defects, we suppose that the defect size is the same in bending and torsional samples which results in a simple translation of the projected effective area $\sqrt{area_p} = \frac{\sqrt{2}}{2}\sqrt{area}$. With the proportional relationship in Eq. (3), the ratio between bending and torsional fatigue strengths can be deduced from Eqs. (4) and (5) shown in Eq. (6). The formula of F_{II} is given in Eq. (7) from the work of Endo and Yanase [46].

$$\frac{\sigma_w}{\tau_w} \cong 1.63F_{II} \tag{6}$$

$$F_{II} = 0.0957 + 2.11\left(\frac{b}{a}\right) - 2.26\left(\frac{b}{a}\right)^2 + 1.09\left(\frac{b}{a}\right)^3 - 0.196\left(\frac{b}{a}\right)^4 \left(0.1 < \frac{b}{a} < 2\right) \tag{7}$$

It can be seen that the ratio between bending and torsional fatigue strengths is strongly dependent on the aspect ratio. Via the staircase method presented in section 3, we have obtained the fatigue strengths under bending and torsion loading. The ratios in different surface conditions are 0.71, 0.81, 0.80 for AB, SP, and TP cases, respectively.

Let us recall that the defects observed on the fracture surfaces are such that the single LoF defect is elongated and penetrating deeply into the volume which leads to a high aspect ratio b/a whilst the cluster of defects is arranged parallelly along with the surface and, if they are considered as one large defect, it is wide-open resulting in a low aspect ratio. As it is unfeasible to measure exactly the defects in the torsional samples because on one hand the observed fracture surface is inclined and on the other hand the LoF defects were sometimes torn apart during loading, we use defects found in the bending samples and only use the estimated aspect ratios to perform some qualitative analyses.

Regarding one single defect, the aspect ratio is often larger than 1 because the virtual crack is more pronounced in depth. For all TP, SP, AB samples, no matter how many defects are present at the initiation site, the largest defect always has the typical morphology as has been schematically shown in Fig. 16. Thus, this kind of defect has an estimated aspect ratio of about 1–2 and it holds correct for all the 3 configurations. But for the multiple defects, it is the opposite. For instance, 4 defects neighboring each other near the surface will yield a virtual crack having a notable width several times larger than the depth. A schematic is also presented in Fig. 16. From Table 5, we know that the extreme case in SP samples is that 8 clustering defects exhibited at the crack initiation site. Hence, the virtual crack from multiple defects has a quite low aspect ratio. Generally, for the continuous defects on the surface in AB samples, the aspect ratio is about 0.1–1 and it is slightly smaller in SP samples with an estimate of about 0.2–2. For the TP cases, the estimated aspect ratio is generally about 0.5–2. Because multiple defects were not always the case for TP samples, it is possible that the estimated aspect ratio is larger than 1 where there is only one deep-penetrating defect found.

In Fig. 16, we plot the fatigue strength ratios versus different aspect ratios. The ellipses denote the predicted fatigue strength ratios with respect to the estimated aspect ratios of different configurations. For instance, the virtual crack originated from the multiple defects in AB condition has an estimated aspect ratio of about 0.1–1 which yields a prediction of fatigue strength ratio of about 0.6–1.35. The fatigue strength ratios measured from the experiments of AB, SP, and TP samples are also provided as star characters in Fig. 16. The proposed method to measure the multiple defects as one is effective to reflect the experimental finding that the torsional fatigue strength is higher than the bending fatigue strength. However, it is noted that the experimental value of the ratio σ_w/τ_w of the TP cases is not distinct from that of the SP cases while the estimated aspect ratios in TP and SP cases vary. This is possibly because the torsion samples, especially the total-polished, exhibit comparable fatigue performances with the machined counterparts. Therefore, the TP cases may not still follow the rule established for the defect-containing materials. For the AB and SP samples, the low aspect ratio of the virtual crack implies that the multiple defects contribute simultaneously when triggering the defect initiation. To conclude, it is plausible to treat the clustering surface/subsurface defects as one large virtual crack in LPBF 316L when considering the fatigue performance in a general sense.

6. Conclusions

With the comprehensive experimental campaign of fatigue tests for the AM steel 316L regarding the effects of the surface defect and loading modes, a series of conclusions can be drawn:.

(1) Despite the absence of the contouring step in our process, the surface roughness of our specimens is consistent with the literature data. Tomography shows that the fabricated material has a very good density (>99.95%).
(2) The fatigue strengths are impaired due to the presence of a lot of (sub)surface LoF defects which may be resulted from the intentionally omitted contouring step during fabrication. In the meantime, the effect of stress gradient seems to be masked by the surface effect.
(3) By removing a thick layer of the surface to get rid of the surface defect to the greatest extent, the fatigue strength under bending/tension loading is not recovered to the expected level as high as that of the wrought material. But the torsional fatigue strength is found slightly higher than those of the machined LPBF or wrought counterparts.
(4) Because the as-built samples have many inherent defects, surface treatment can improve the fatigue performances in all the 3 tested loading configurations: bending, tension, and torsion. But the improvement is seen much more pronounced in bending/tension than in torsion. That is to say, the surface effect is more critical in bending/tension loadings.
(5) Even if the LPBF as-built 316L torsional samples have a very poor surface state, it is confirmed for the first time that the presence of AM inherent defects does not change the mechanism in torsional fatigue failure. The crack is initiated by the defects in Mode II during Stage I and the Mode I crack is predominant only in Stage II.
(6) By using the Murakami approach regarding the relationship between fatigue strength and defect size as well as the fatigue strength ratio in different loading modes, it is found that the multiple clustering defects act synergistically as one large defect to initiate the fatigue crack.

Declaration of Competing Interest

The authors declare that they have no known competing financial interests or personal relationships that could have appeared to influence the work reported in this paper.

Acknowledgment

The authors would like to thank Nikita Dorofeev and Marco Scarpetta for their earnest help in conducting the experiments.

References

[1] Yap CY, Chua CK, Dong ZL, Liu ZH, Zhang DQ, Loh LE, et al. Review of selective laser melting: materials and applications. Appl Phys Rev 2015;2(4):041101. https://doi.org/10.1063/1.4935926.

[2] Montero-Sistiaga ML, Godino-Martinez M, Boschmans K, Kruth JP, Van Humbeeck J, Vanmeensel K. Microstructure evolution of 316L produced by HP-SLM (high power selective laser melting). Addit Manuf 2018;23:402–10. https://doi.org/10.1016/j.addma.2018.08.028.

[3] Song Y, Sun Q, Guo K, Wang X, Liu J, Sun J. Effect of scanning strategies on the microstructure and mechanical behavior of 316L stainless steel fabricated by selective laser melting. Mater Sci Eng A 2020;793:139879. https://doi.org/10.1016/j.msea.2020.139879.

[4] Salman OO, Gammer C, Chaubey AK, Eckert J, Scudino S. Effect of heat treatment on microstructure and mechanical properties of 316L steel synthesized by selective laser melting. Mater Sci Eng A 2019;748:205–12. https://doi.org/10.1016/j.msea.2019.01.110.

[5] Dryepondt S, Nandwana P, Fernandez-Zelaia P, List F. Microstructure and high temperature tensile properties of 316L fabricated by laser powder-bed fusion. Addit Manuf 2021;37:101723. https://doi.org/10.1016/j.addma.2020.101723.

[6] Spierings AB, Starr TL, Wegener K. Fatigue performance of additive manufactured metallic parts. Rapid Prototyp J 2013;19(2):88–94. https://doi.org/10.1108/13552541311302932.

[7] Solberg K, Guan S, Razavi SMJ, Welo T, Chan KC, Berto F. Fatigue of additively manufactured 316L stainless steel: the influence of porosity and surface roughness. Fatigue Fract Eng Mater Struct 2019;42(9):2043–52. https://doi.org/10.1111/ffe.13077.

[8] Davies CM. Fatigue crack initiation and growth behavior of 316L stainless steel manufactured through selective laser melting. In: Proc ASME 2017 press vessel pip conf, Hawaii, USA; 2017. p. 1–7.

[9] Uhlmann E, Fleck C, Gerlitzky G, Faltin F. Dynamical fatigue behavior of additive manufactured products for a fundamental life cycle approach. Proc CIRP 2017;61:588–93. https://doi.org/10.1016/j.procir.2016.11.138.

[10] Elangeswaran C, Cutolo A, Muralidharan GK, de Formanoir C, Berto F, Vanmeensel K, et al. Effect of post-treatments on the fatigue behaviour of 316L stainless steel manufactured by laser powder bed fusion. Int J Fatigue 2019; 123: 31–9. <https://doi.org/10.1016/j.ijfatigue.2019.01.013>.

[11] Shrestha R, Simsiriwong J, Shamsaei N. Fatigue behavior of additive manufactured 316L stainless steel parts: Effects of layer orientation and surface roughness, Addit Manuf 2019; 28: 23–38. <https://doi.org/10.1016/j.addma.2019.04.011>.

[12] Bryson WE. Heat treatment, selection, and application of tool steels. In: Heat treat sel appl tool steels. Carl Hanser Verlag GmbH & Co. KG, München; 2005. p. I–XV. <https://doi.org/10.3139/9783446436701.fm>.

[13] Riemer A, Leuders S, Thöne M, Richard HA, Tröster T, Niendorf T. On the fatigue crack growth behavior in 316L stainless steel manufactured by selective laser melting. Eng Fract Mech 2014;120:15–25. https://doi.org/10.1016/j.engfracmech.2014.03.008.

[14] Leuders S, Lieneke T, Lammers S, Tröster T, Niendorf T. On the fatigue properties of metals manufactured by selective laser melting – the role of ductility. J Mater Res 2014;29(17):1911–9. https://doi.org/10.1557/jmr.2014.157.

[15] Mower TM, Long MJ. Mechanical behavior of additive manufactured, powder-bed laser-fused materials. Mater Sci Eng A 2016;651:198–213. https://doi.org/10.1016/j.msea.2015.10.068.

[16] Liverani E, Toschi S, Ceschini L, Fortunato A. Effect of selective laser melting (SLM) process parameters on microstructure and mechanical properties of 316L austenitic stainless steel. J Mater Process Technol 2017;249:255–63. https://doi.org/10.1016/j.jmatprotec.2017.05.042.

[17] Blinn B, Ley M, Buschhorn N, Teutsch R, Beck T. Investigation of the anisotropic fatigue behavior of additively manufactured structures made of AISI 316L with short-time procedures PhyBaL LIT and PhyBaL CHT. Int J Fatigue 2019;124:389–99. https://doi.org/10.1016/j.ijfatigue.2019.03.022.

[18] Zhang M, Sun C-N, Zhang X, Goh PC, Wei J, Hardacre D, et al. Fatigue and fracture behaviour of laser powder bed fusion stainless steel 316L: Influence of processing parameters. Mater Sci Eng A 2017;703:251–61. https://doi.org/10.1016/j.msea.2017.07.071.

[19] Andreau O, Pessard E, Koutiri I, Penot J-D, Dupuy C, Saintier N, et al. A competition between the contour and hatching zones on the high cycle fatigue behaviour of a 316L stainless steel: analyzed using X-ray computed tomography. Mater Sci Eng A 2019;757:146–59. https://doi.org/10.1016/j.msea.2019.04.101.

[20] Afkhami S, Dabiri M, Alavi SH, Björk T, Salminen A. Fatigue characteristics of steels manufactured by selective laser melting. Int J Fatigue 2019;122:72–83. https://doi.org/10.1016/j.ijfatigue.2018.12.029.

[21] Yang T, Liu T, Liao W, MacDonald E, Wei H, Chen X, et al. The influence of process parameters on vertical surface roughness of the AlSi10Mg parts fabricated by selective laser melting. J Mater Process Technol 2019;266:26–36.

[22] Chen Z, Wu X, Tomus D, Davies CHJ. Surface roughness of selective laser melted Ti-6Al-4V alloy components. Addit Manuf 2018;21:91–103. https://doi.org/10.1016/J.ADDMA.2018.02.009.

[23] Bourell D, Spierings AB, Herres N, Levy G. Influence of the particle size distribution on surface quality and mechanical properties in AM steel parts. Rapid Prototyp J 2011;17(3):195–202. https://doi.org/10.1108/13552541111124770.

[24] Dewidar MM, Khalil KA, Lim JK. Processing and mechanical properties of porous 316L stainless steel for biomedical applications. Trans Nonferrous Met Soc China (English Ed) 2007;17(3):468–73. https://doi.org/10.1016/S1003-6326(07)60117-4.

[25] Liu X, Chu P, Ding C. Surface modification of titanium, titanium alloys, and related materials for biomedical applications. Mater Sci Eng R Reports 2004;47(3-4):49–121.

[26] Roland T, Retraint D, Lu K, Lu J. Fatigue life improvement through surface nanostructuring of stainless steel by means of surface mechanical attrition treatment. Scr Mater 2006;54(11):1949–54.

[27] Puchi-Cabrera ES, Matínez F, Herrera I, Berríos JA, Dixit S, Bhat D. On the fatigue behavior of an AISI 316L stainless steel coated with a PVD TiN deposit. Surf Coat Technol 2004;182(2–3):276–86. https://doi.org/10.1016/j.surfcoat.2003.07.003.

[28] Guerchais R, Morel F, Saintier N, Robert C. Influence of the microstructure and voids on the high-cycle fatigue strength of 316L stainless steel under multiaxial loading. Fatigue Fract Eng Mater Struct 2015;38:1087–104. https://doi.org/10.1111/ffe.12304.

[29] Sanaei N, Fatemi A. Defects in additive manufactured metals and their effect on fatigue performance: a state-of-the-art review. Prog Mater Sci 2021;117:100724. https://doi.org/10.1016/j.pmatsci.2020.100724.

[30] Wang Y, Su Z. Effect of micro-defects on fatigue lifetime of additive manufactured 316L stainless steel under multiaxial loading. Theor Appl Fract Mech 2021;111:102849. https://doi.org/10.1016/j.tafmec.2020.102849.

[31] Wang Y, Wang W, Susmel L. Constant/variable amplitude multiaxial notch fatigue of additively manufactured AISI 316L. Int J Fatigue 2021;152:106412. https://doi.org/10.1016/j.ijfatigue.2021.106412.

[32] Schijve J, editor. Fatigue of structures and materials. Dordrecht: Springer Netherlands; 2009.

[33] Zhang J, Fatemi A. Surface roughness effect on multiaxial fatigue behavior of additive manufactured metals and its modeling. Theor Appl Fract Mech 2019;103:102260. https://doi.org/10.1016/j.tafmec.2019.102260.

[34] Fatemi A, Molaei R, Sharifimehr S, Phan N, Shamsaei N. Multiaxial fatigue behavior of wrought and additive manufactured Ti-6Al-4V including surface finish effect. Int J Fatigue 2017;100:347–66. https://doi.org/10.1016/j.ijfatigue.2017.03.044.

[35] Molaei R, Fatemi A. Crack paths in additive manufactured metallic materials subjected to multiaxial cyclic loads including surface roughness, HIP, and notch effects. Int J Fatigue 2019;124:558–70. https://doi.org/10.1016/j.ijfatigue.2019.03.007.

[36] Stoffregen HA, Butterweck K, Abele E. Fatigue analysis in selective laser melting: review and investigation of thin-walled actuator housings. In: Int solid free fabr symp, University of Texas at Austin; 2014. p. 635–650. <https://doi.org/10.26153/TSW/15713>.

[37] DebRoy T, Wei HL, Zuback JS, Mukherjee T, Elmer JW, Milewski JO, et al. Additive manufacturing of metallic components – process, structure and properties. Prog Mater Sci 2018;92:112–224. https://doi.org/10.1016/j.pmatsci.2017.10.001.

[38] Wentzel H, Huang X. Experimental characterization of the bending fatigue strength of threaded fasteners. Int J Fatigue 2015;72:102–8. https://doi.org/10.1016/j.ijfatigue.2014.11.005.

[39] El Khoukhi D, Morel F, Saintier N, Bellett D, Osmond P, Le V-D, et al. Experimental investigation of the size effect in High Cycle Fatigue: role of the defect population in cast aluminium alloys. Int J Fatigue 2019;129:105222. https://doi.org/10.1016/j.ijfatigue.2019.105222.

[40] Le VD, Saintier N, Morel F, Bellett D, Osmond P. Investigation of the effect of porosity on the high cycle fatigue behaviour of cast Al-Si alloy by X-ray micro-tomography. Int J Fatigue 2018;106:24–37. https://doi.org/10.1016/j.ijfatigue.2017.09.012.

[41] Lee Y-L, Barkey ME, Kang H-T. Metal fatigue analysis handbook: practical problem-solving techniques for computer-aided engineering. Butterworth-Heinemann; 2011. https://books.google.com/books?id=_EDNz9zv-0MC&pgis=1 (accessed November 14, 2021.

[42] Koutiri I, Pessard E, Peyre P, Amlou O, De Terris T. Influence of SLM process parameters on the surface finish, porosity rate and fatigue behavior of as-built Inconel 625 parts. J Mater Process Technol 2018;255:536–46. https://doi.org/10.1016/j.jmatprotec.2017.12.043.

[43] Romano S, Miccoli S, Beretta S. A new FE post-processor for probabilistic fatigue assessment in the presence of defects and its application to AM parts. Int J Fatigue 2019;125:324–41. https://doi.org/10.1016/j.ijfatigue.2019.04.008.

[44] Le VD, Pessard E, Morel F, Edy F. Interpretation of the fatigue anisotropy of additively manufactured TA6V alloys via a fracture mechanics approach. Eng Fract Mech 2019;214:410–26. https://doi.org/10.1016/j.engfracmech.2019.03.048.

[45] Houria I. Etude expérimentale et modélisation de la durée de vie en fatigue d ' un alliage d ' aluminium de fonderie A356-T6 sous chargement multiaxial. ISAE-ENSMA Ecole Nationale Supérieure de Mécanique et d'Aérotechique – Poitiers; 2015.

[46] Endo M, Yanase K. Crack path and threshold condition for small fatigue crack growth in annealed carbon steels under fully-reversed torsional loading. Int J Fatigue 2019;125:112–21. https://doi.org/10.1016/j.ijfatigue.2019.03.027.

[47] Murakami Y. Metal fatigue:effects of small defects and nonmetallic inclusions. Elsevier Science Ltd, Oxford; 2002.